Arch. Metall. Mater. **70** (2025), 2, 803-817

DOI: https://doi.org/10.24425/amm.2025.153483

N. MUTHUKUMARAN[1*], B. ARULMURUGAN[1], R. SURESHKUMAR[2], R. BHARATHIKANNA[3]

# EVALUATION OF MICROSTRUCTURE, AND MECHANICAL PROPERTIES OF SUPERALLOY 59 AND 904L DISSIMILAR WELDS USING HOT WIRE TURBO TIG

This research involves the dissimilar welding of a novel combination of superalloy 59 and 904L using Hot Wire Turbo TIG welding (HWTT) with ERNiCrMo-13 filler wire. Macroscopic examination revealed defect-free welds with optimized geometry and minimal heat-affected zone. The bead geometry, influenced by capillary action and the Marangoni effect, exhibited a 7 mm crest width, 5.5 mm center width, and 2.6 mm depth. Microstructural analysis through FESEM and EDS revealed a substantial 32.06% Mo-enriched secondary phase in the fusion zone, vital for structural reliability and enhancing weldment mechanical properties. Hardness testing revealed 15% higher values in the weld joint compared to base metals. Cryogenic treatment enhanced the weldment tensile strength by up to 10%, with deep cryogenic treatment (DCT) surpassing as-welded samples by 9.5%. Tensile and impact tests, along with fractography images, revealed microstructure-influenced ductile fractures. Charpy impact toughness of the weld fusion zone, at 89 J, showcases favorable properties, 2% lower than alloy 59 but 11.2% higher than 904L, attributed to DCT.

*Keyword:* Hot wire Turbo TIG; Dissimilar welding; superalloy 59; 904L; Cryogenic treatment

## 1. Introduction

Alloy 59, or UNS N06059, is a high-performance superalloy composed of 59% nickel, 23% chromium, and 16% molybdenum, with 2% minor alloying elements [1]. It's known for excellent corrosion resistance, high-temperature stability, oxidation resistance, mechanical strength, and weldability [2]. This makes it a valuable choice in industries such as chemicals, power generation, petrochemicals, and offshore applications [3]. The 904L, an iron-nickel superalloy, excels in dissimilar welding by allowing the joining of different materials while preserving corrosion resistance and mechanical properties [4]. Its versatility and compatibility with various materials, coupled with its ability to match mechanical properties and maintain corrosion resistance in dissimilar welds, make it a top choice for industries like chemical processing, offshore operations, and infrastructure projects that rely on dissimilar welding applications [5,6]. The Hot Wire Turbo TIG (HWTT) welding machine, a variation of GTAW, boosts productivity for welding similar and dissimilar materials like Nickel-based and Iron-Nickel superalloys. It incorporates Industry 4.0 principles for high-speed, stable welding with low heat input and simplified procedures. This machine can store welding programs and interface with CNC machines, ensuring precise control and automation, and aligning with modern industrial practices [7].

Welding dissimilar materials (Ni superalloy and Fe-Ni alloy) is complex due to varying properties [8]. Connecting Industry 4.0 technologies such as data analytics, machine learning, and robotics is key to enhancing welding outcomes [10,11]. These technologies identify defect patterns, predict issues like hot cracking or distortion, and automate welding processes [12,13]. By incorporating HWTT welding into this framework, the quality of dissimilar welds is improved, leading to increased productivity, enhanced safety, and reduced costs [1,14]. In dissimilar welding, researchers address challenges and opportunities by delving into metallurgical interactions, parameter optimization, and advanced processes for high-quality welds. Arivarasu et al. emphasize the benefits of using nickel-based filler wire, ERNiCr-3, in the PC GTAW process, improving tensile strength and weld quality [15]. Naffakh et al. highlight the superiority of Inconel filler material in joining AISI 310 stainless steel to Inconel 657 superalloy [16]. Gao et al. explore the potential of visual sensing and advanced algorithms in improving weld quality in Industry 4.0 [17] Benakis et al. focus on monitoring the welding process for defect detection

---

[1] DEPARTMENT OF MECHANICAL ENGINEERING, KPR INSTITUTE OF ENGINEERING AND TECHNOLOGY, COIMBATORE, TAMIL NADU, 641 407, INDIA
[2] DEPARTMENT OF MECHANICAL ENGINEERING, SRI ESHWAR COLLEGE OF ENGINEERING, COIMBATORE, TAMILNADU, 641 202, INDIA
[3] DEPARTMENT OF AGRICULTURAL ENGINEERING, NEHRU INSTITUTE OF TECHNOLOGY, COIMBATORE, TAMILNADU, 641 105, INDIA

* Corresponding author: nmuthu1966@gmail.com

and characterization, using robotic Gas Tungsten Arc Welding (GTAW) [18]. Parameter selection significantly influences weld quality and structural integrity, especially in dissimilar welding, where base metal and filler material compatibility is crucial for sound welds [19-22]. In the Ni-Cr-Mo system, secondary phases like sigma, chi, laves, and carbides have a notable impact on alloy properties, including mechanical strength, toughness, corrosion resistance, and high-temperature performance [23,24]. Factors such as alloy composition, cooling rate, heat treatment, and elevated temperature exposure influence the formation and stability of these phases [25,26]. Evangeline et al. found that solidification during the cladding process significantly affects the microstructure and corrosion resistance of the Ni-Cr-Mo alloy, particularly due to Nb segregation [27]. Farkoosh et al. demonstrated that intermetallic phases are influenced by alloy composition and solidification [28]. Thermally stable Ni intermetallic enhances yield strength at high temperatures, while Mn improves creep resistance and ductility. Yan et al. highlighted the influence of welding processes on joint microstructure and mechanical properties, with welding parameters affecting transition zones and heat-affected zones (HAZ) [29]. Laser welding and laser-TIG hybrid welding are recommended for industrial applications due to their speed and mechanical properties. Ramkumar et al. reported that GTAW welding with ENiCu7 and E309L filler wires produces satisfactory joints between AISI 304 and Monel 400, with identified secondary phases impacting mechanical properties and corrosion resistance [30].

Cryogenic treatment, which involves exposing materials to extremely low temperatures, offers two modes: shallow and deep. Shallow mode cools samples to –80°C to –120°C, providing stress relief, improved dimensional stability, and enhanced wear resistance [31,32]. Deep cryogenic treatment goes below –150°C with longer soaking times, leading to structural changes like carbide precipitation and more stable martensitic structures [33-35]. The choice between shallow and deep cryogenic treatments depends on material and application needs [36]. In this study, we investigate the dissimilar joint between Nickel superalloy 59 and Fe-Ni superalloy 904L, a relatively unexplored pair of materials, making it a unique aspect of our work. We used the HWTT welding process, an emerging variant of GTAW that enables rapid welding, increasing productivity, and is well-suited for Industry 4.0 automation. Additionally, the study investigates the potential benefits of cryogenic treatment on the mechanical characteristics of the weldment to enhance its performance under tensile stresses and impact load absorption.

## 2. Experimental procedure

The spectroscopic analysis verified the elemental composition of superalloy 59 and 904L. The elemental composition and their physical properties are depicted in TABLE 1 and TABLE 2 respectively [37]. The samples (150×55×3 mm) prepared with a Wire Cut EDM machine displayed in Fig. 1(a) and Fig. 1(b) depicts the Cryogenic Treatment Cycle, offering a visual representation of the sequential stages and key parameters employed in our study. This illustration provides valuable insights into the experimental conditions crucial for material analysis The specimens welded using Filler wire ENMiCr-13 and a HWTT welding machine at a torch speed of 130 mm/min with Argon gas protection after cleaning the specimens with acetone.

Fig. 2(a-h) presents the HWTT machine setup, featuring TIG and hot power functions. Super imposition arrangement allows wire drag and forward motion during welding. The heat source precisely heats the filler wire to 650°C, corresponding to approximately 50% of its melting range, as an essential parameter in the HWTT process. This specific temperature is carefully controlled to optimize the welding conditions.

TABLE 1

Elemental compositions of alloy 59 and 904L

| Base/Filler Metal | Chemical Composition (% wt.) | | | | | | | | |
|---|---|---|---|---|---|---|---|---|---|
| | Ni | Mo | Cr | Cu | Mn | Fe | Si | C | Others |
| Alloy 59 | 57-59 | 15-16 | 22-24 | 0.5 | 0.5 | <1.0 | 0.1 | 0.01 | 0.1 (S), 0.1 (Al), 0.04 (P) 0..3(Co) |
| 904L | 23-28 | 4-5 | 19-23 | 1-2 | 2.0 Max | 38.0 Max | 1.0 | 0.005 | 0.035 (S), 0.015 (P), 0.02 (Si) |
| ERNiCrMo-13 | 59 | 16.0 | 23.0 | 0.5 | 0.30 | 0.5 | 0.005 | 0.005- | 0.015 (P), 0.1 (Al), 0.01 (S), 0.3 (Co) |

TABLE 2

Physical properties of alloy 59,904L and filler wire

| Properties | Alloy 59 | 904L | ERNiCrMo-13 |
|---|---|---|---|
| Conductivity | 10.4 W/m K | 11.5 W/m K | 10.4 W/m K |
| Co-efficient of Thermal Expansion | $12.0\times10^{-6}$cm/cm/°C | $15.3\times10^{-6}$ cm/cm/°C | $12.0\times10^{-6}$ cm/cm/°C |
| Density | 8.6 g /cm$^3$ | 7.95 g /cm$^3$ | 8.6 g /cm$^3$ |
| Elastic Modulus | 210 Giga Pascal | 190 Giga Pascal | 210 Giga Pascal |
| Electric Resistivity | 126 μ Ω cm | 95.2 μ Ω cm | 126 μ Ω cm |
| Elongation | 40% | 36% | 40-47% |
| Melting Temperature | 1310-1360°C | 1,350°C | 1310-1360°C |
| Tensile Strength | 690 MPa | 490 MPa | 690 MPa |
| Yield Strength | 380 MPa | 280 MPa | 380 MPa |

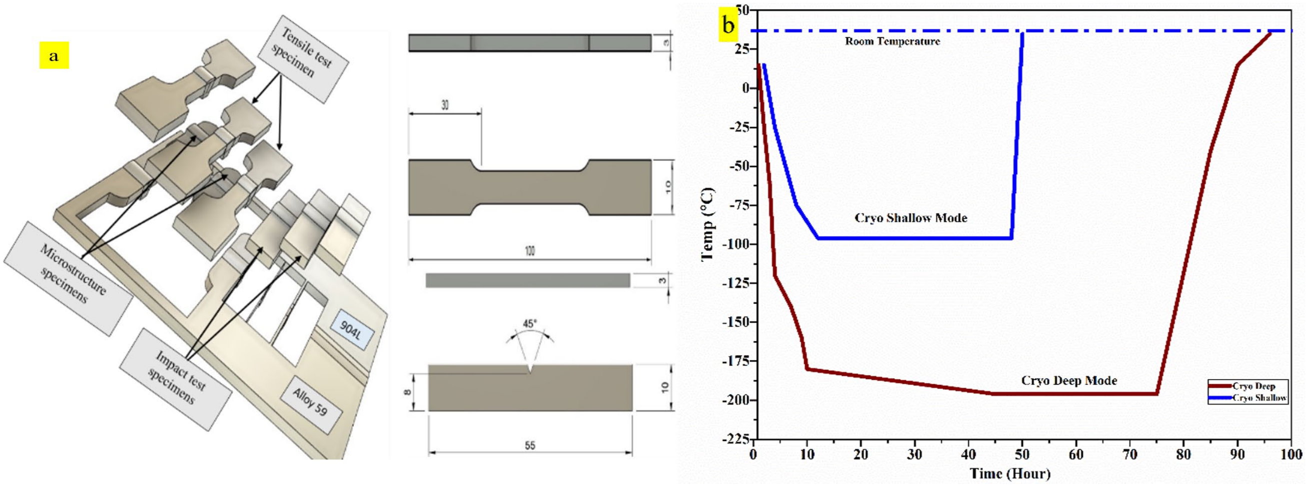

Fig. 1. (a) Specimen preparation as per ASTM standard using Electrical Discharge Machining (EDM) from dissimilar weldment. (b) Cryogenic treatment cycle

Fig. 2. Hot wire TIG welding machine working (a to h) Machine set-up; i) Process sequence

TABLE 3

The process parameters used for hot wire Turbo TIG welding

| Process Variables | Setting Value |
|---|---|
| Voltage | 24 V |
| Current | 200 A |
| Wire speed | 130 mm/min |
| Pulse Frequency | 15 Hz |
| Pre-Gas Flow Rate | 10 liter per second |
| Post – Gas Flow Rate | 15 liter per Second |
| Protecting gas | Ar (Argon) |
| Heat Input | 0.61 KJ/mm |

Fig. 2(a), 2(b) depicts the turbo power unit provides a tailored shielding gas atmosphere, reducing heat input and improving weld bead quality. Fig. 2(c), 2(d) and 2(e) presents the hot wire feed unit, automatic travel speed mechanism and monitoring device attachment respectively. Fig. 2(g) and 2(h) shows the monitoring sensor and control station. The HWTT welding process sequence with pre- and post-gas flows for 2 seconds and 4 seconds respectively illustrated in Fig. 2(i).

The selected process parameters for HWTT welding out lined in TABLE 3. After HWTT welding with ERNiCrMo-13 filler wire for dissimilar joints, conducted a thorough examination to assess microstructure and mechanical integrity. The Wire Cut Electrical Discharge Machining (WCEDM) used to craft transverse sections for microstructure analysis. Composite sections (CS) of dimensions 28 mm × 5 mm × 3 mm, comprising Base Metal (BM) 1 + Weld Interface (WI)1 + Fusion Zone + WI 2 + BM 2, were prepared for further analysis. The microstructural examination involved several steps. The CS was polished using SiC Emery sheets from 220 to 2000 grit. Subsequently, alumina mixed with water was applied for velvet-cloth-covered disc polishing to achieve a mirror-like finish. Metallography analysis followed to examine the microstructures. For Ni superalloy 59 and the fusion zone, the polished CS were etched using 10% oxalic acid mixture with a 9 V electrolyte etching for 60 seconds. The 904L's microstructures were made visible using a solution of 4% nitric acid with alcohol and a 1:5:5 ratio of copper sulfate and HCL acid aqueous solution by swapping. The weld CS were examined using a Carl Zeiss Optical microscope. Elemental composition analysis was carried out in triplicate at each zone with a Zeiss Smart EDS analyzer using a Field Emission Scanning Electron Microscope (FESEM). The reported results represent the average of three trials, and standard deviation values were calculated to assess the precision and confidence of the measurements. Vickers micro-hardness testing measured hardness throughout the weld depth with a 0.5 kg load with 3 seconds delay time as per ASTM E384.Tensile and impact testing followed ASTM standards E8 and E23 on specimens cut from welded plates using EDM wire cutting. These samples were cryogenically treated, with two modes: shallow and deep. Shallow treatment involved gradual cooling to –80°C to –90°C for 48 hours and reheating, providing stress relief and wear resistance. Deep treatment involved exposure to temperatures below –196°C for 96 hours, followed by gradual reheating up to room temperature. Charpy V-notch tests were conducted on As-welded, Cryogenic shallow, and Deep mode samples, following ASTM standards E8 and E23. FESEM Fractography studies were conducted to investigate fracture modes, and results were reliably reproduced in triplicate. The HWTT welding process with ERNiCrMo-13 filler wire was conducted throughout the experimental procedure.

## 3. Results and discussion

### 3.1. Base Metals Investigation

The Alloy 59 base metal (BM) micrograph in the solution-annealed state, as depicted in Fig. 3(a). The presence of an austenitic matrix rich in nickel (Ni) and featuring annealing twin formations was revealed. These twins indicate a desirable characteristic of mechanical properties [38]. The microstructure of the 904L base metal reveals a homogeneous austenitic structure, suggesting that the solution annealing process effectively eliminated impurities, facilitated uniform alloy composition, and resulted in a predominantly austenitic microstructure exposed in Fig. 3(b). Additionally, the microstructure confirms that the material maintains the same crystal structure or phase throughout the cooling process without undergoing significant structural changes due to the absence of polymorphic transformations during cooling [39].

### 3.2. Macroscopic examination

Substantial evidence of the characteristics, quality, and penetration of the weld joint was obtained through a macroscopic examination of HWTT welds produced using ERNiCrMo-13 filler wire for dissimilar welding. The cross-sectional view of the weldment is presented in Fig. 3(c). The weldment with a narrow bead width and adequate penetration is achieved by using HWTT welding with pulsed current, a turbo unit preheating filler wire by 50%, and maintaining a protective gas environment. Minimized shear stress, optimal solidification, and fewer heat-affected zones are the results of lower heat input in pulsed mode, balanced driving forces, and steady fluid flow at the weld pool. Pulse mechanisms in HWTT welding, involving controlled filler wire heating and droplet formation, provide precise control over droplet transfer through pinch and gravitational forces. The added stability achieved via the turbo unit in HWTT further enhances the welding process. This control significantly influences the weld pool characteristics, such as volume, size, and shape, ultimately impacting crucial mechanical properties like weld pool width. These factors collectively contribute to the overall weld quality and performance in Hot Wire Turbo TIG welding.

The HWTT welding can enhance the weld geometry parameters, including bead width at Crest 7 mm, 5.5 mm at the center, 3.2 mm at root, depth 2.6 mm, and depth-to-width ratio, consistent with observations made by Sun et al. [40]. The wider width at the crest and narrower widths below it and the root, which are charac-

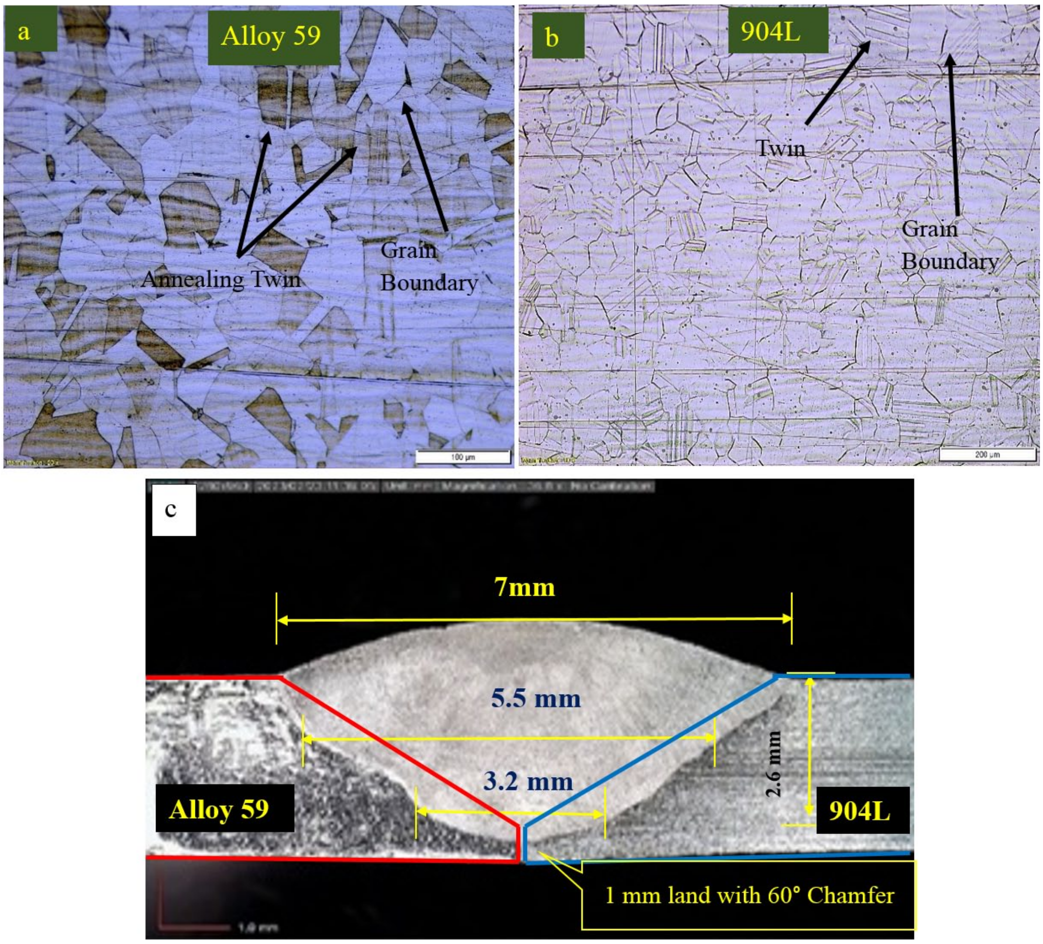

Fig. 3. Optical micro and macro structure of base metals a) Alloy 59 b) 904L and c) Cross section of weldment made with HWTT process with ERNiCrMo-13 Filler

teristic of the observed bead geometry, are influenced by capillary action and buoyancy forces. The temperature gradient during welding leads to the Marangoni effect, resulting in the broader bead geometry at the Crest and narrower bead geometry in the middle and end regions [41]. The observed bead geometry shows the minimal heat-affected zone (HAZ), one crucial region in welding processes that affects microstructural changes, mechanical properties, and welding integrity [42]. Incorporating a turbo unit and gas protection for controlled heat inputs, HWTT welding ensures a regulated solidification process, yielding fine equiaxed dendrite structures. This approach minimizes grain coarsening in the heat-affected zone (HAZ), addresses Mo and Ni segregation, and prevents secondary phase precipitation, resulting in refined microstructures and reduced microsegregation. The elimination of hot cracking in the weldments is confirmed, and the reduction in microsegregation of alloying elements around grain boundaries indicates the absence of hot cracking due to its lower heat input, 0.61 KJ/mm, compared to other GTAW counterparts [43].

### 3.3. Microstructural analysis

Microscopic examination evaluated the weld integrity ensuring a sound metallurgical bond between Alloy 59 and 904L. The HWTT welding and ERNiCrMo-13 filler wire facilitate rapid solidification and minimal thermal accumulation contributing to the weld quality. Interfacial microstructures between 904L, Alloy 59, and Fusion Zone shown in. Fig. 4(a), 4(b), and 4(c). The weld interfaces on both the alloy 59 side Fig. 4(b) and the 904L side Fig. 4(a) exhibit columnar dendrites. Negligible grain growth was observed in the HAZ of alloy 59 attributed to its high nickel content and low thermal conductivity compared to 904L.

Additionally, Fig. 4(a) reveals noticeable grain coarsening adjacent to the heat affected zone (HAZ) in the alloy 904L weld interface. Furthermore, as illustrated in Fig. 4(a) there is no evidently un-mixed region between the Weld Interface and the HAZ on the 904L side. This absence of an unmixed zone highlights the favorable compatibility between 904L and ERNiCrMo-13 filler metal. However, a distinctive crescent shape refers to as the ‘peninsula’ region was identified at the interface of the 904L side, as inferred from Fig. 4(a). In dissimilar metal welds, peninsula may form if the bulk weld pool’s composition is different from the base metals [44]. A temperature gradient is produced along the weld pool boundary by this compositional difference with the base metal interface experiencing a lower temperature. This can lead to the formation of an unmixed liquid metal layer at the interface, which can solidify fast before interfacing significantly with the surrounding liquid. This quick solidification may

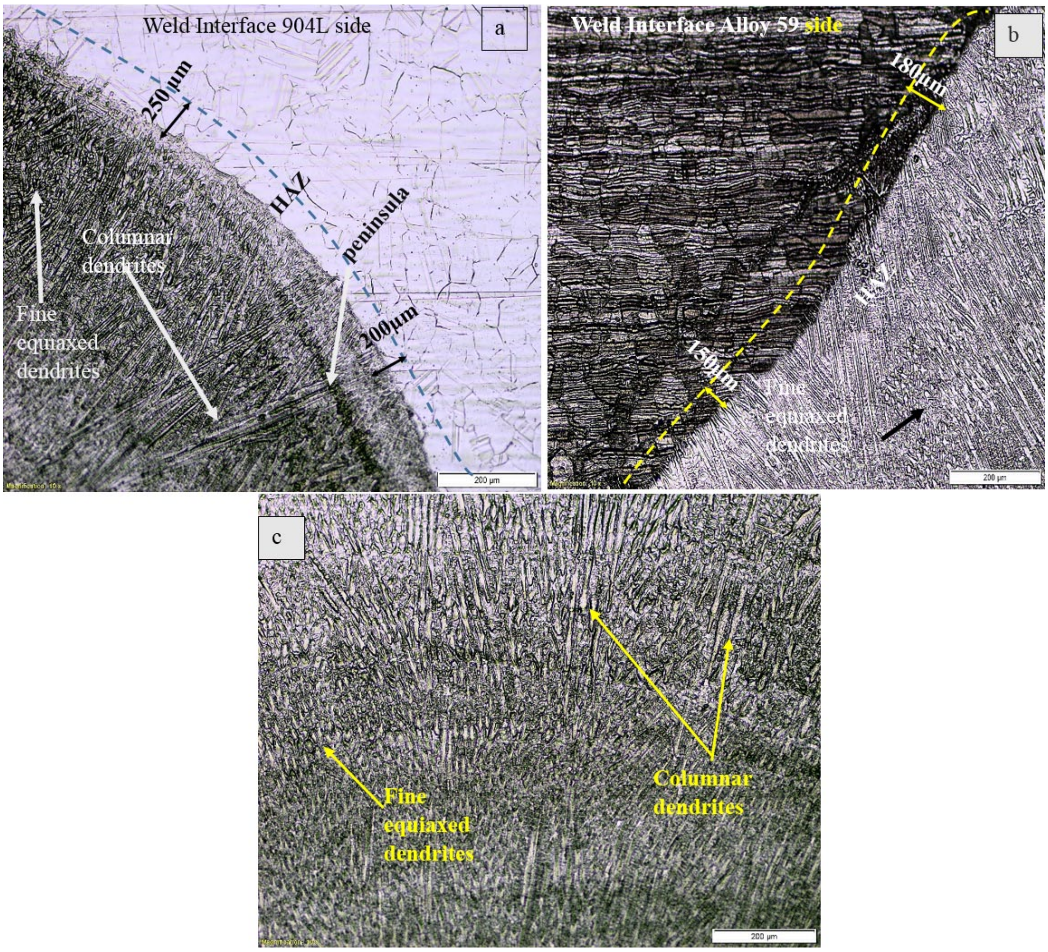

Fig. 4. Optical microstructure image of dissimilar weld made by HWTT with ERNiCrMo-13 Filler a) Weld interface 904L side b) Weld interface alloy 59 side c) Weld center

cause a peninsula to form. Formation of peninsulas in welding results from differences in composition between the bulk weld pool and the base metal. When the liquidus temperature of the bulk weld pool is lower than that of the base metal temperature, leading to a non-isothermal pool boundary, the solidification front shifts backward. This backward shift creates a cooler region ahead of the solidification front. The rapid freezing of the layer of unmixed liquid metal within this cooler region gives rise to peninsulas. This phenomenon underscores the intricate interplay of composition, solidification, and convection in the welding process [45].

Peninsulas show good weld quality when they are present in dissimilar metal welds. Peninsulas are a sign that a strong and continuous interface has been formed as a result of good wetting and spreading between the base and filler metals. It can also enhance the mechanical qualities of the weld by preventing the formation of harmful phases and fine tuning the grain structure. The microstructure at the weld center, revealing a transition from a columnar structure to fine equiaxed dendrites spanning from the weld interface (WI) to the fusion zone (FZ) illustrates in Fig. 4(c). This transition is attributed to the unique turbo power utilizing to heat the wire 50% of its melting range aids to reduce overall heat input of the HWTT welding. The lower heat input permits the equiaxed grains grow and solidify causes to more uniform distribution of grain orientations. The higher cooling rates at the fusion boundary promote the growth of columnar dendrites in a direction perpendicular to the heat flow, while the lower cooling rates at the weld center favor the formation of equiaxed dendrites. Improved mechanical properties are the outcome of the controlled nucleation strategies that cause the columnar dendrites to become equiaxed grains during the solidification process. Equiaxed grains contribute to better material performance by having a more uniform distribution of stress, increased density at the grain boundary for strength and toughness, and decreased weaknesses associated with anisotropy.

### 3.3.1. SEM/EDS Analysis

The analysis of SEM/EDS revealed clear distinction between the columnar grains dendritic and inter-dendritic regions of the weld fusion zone. The weld fusion zone examined using FESEM and EDS as shown in Fig. 5(a) (i, ii, iii). During the analysis of the fusion zone a secondary phase was observed, accompanied by a notable increase in molybdenum (Mo) content, which is confirmed by EDS spectrum in Fig. 5(iii). The Mo content in the fusion zone significantly increase from 10% to 32%. Typically, 904L has a lower Mo content than alloy 59.

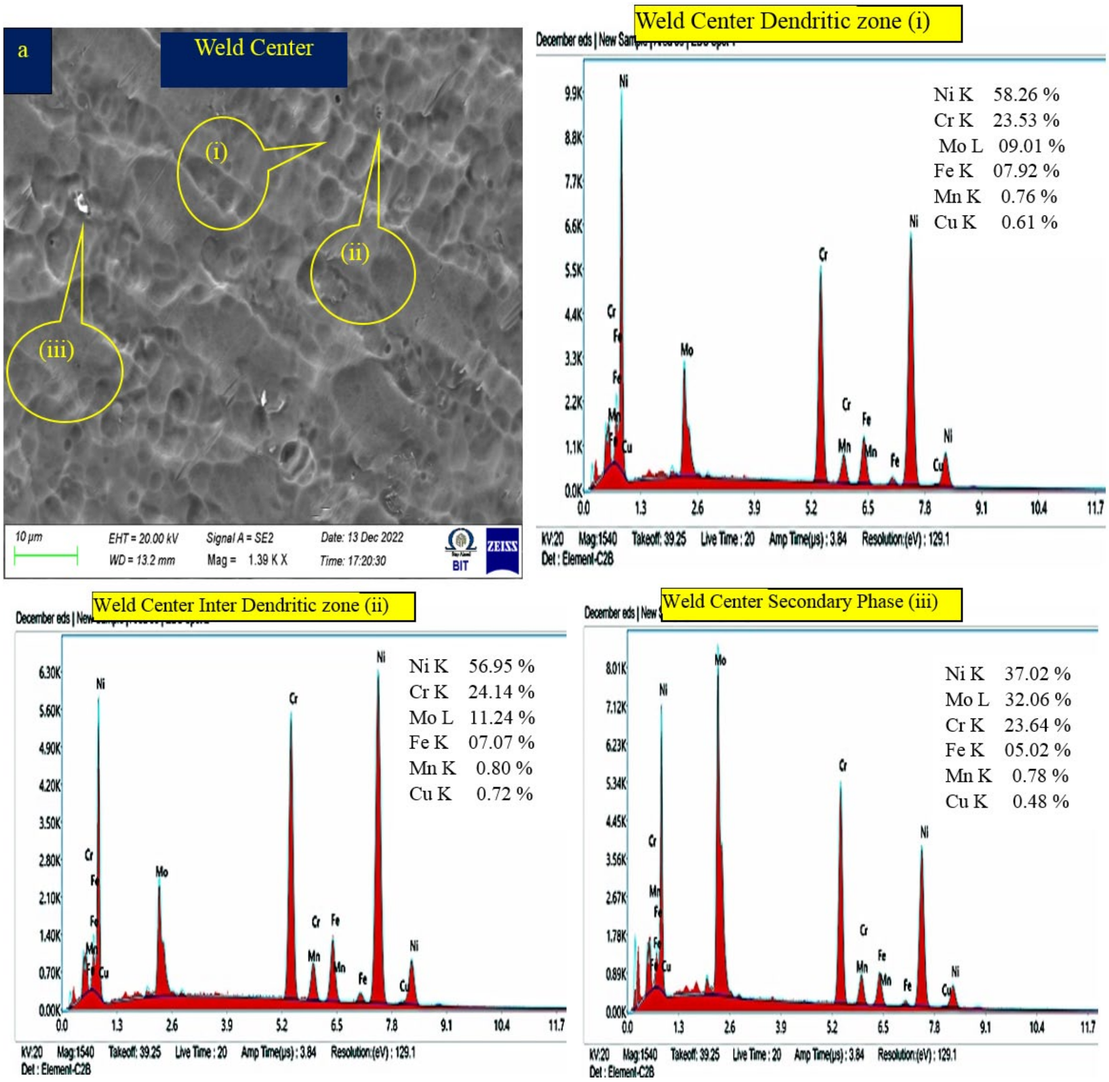

Fig. 5. SEM/EDS analysis of dissimilar weld made by HWTT -ERNiCrMo-13 filler (a) SEM image of weld center and EDS result of (i) Weld center dendritic core; (ii) Weld center inter-dendritic core; (iii) Weld center secondary phase

Mo concentration increases locally during welding as a result of Mo migrating from the alloy 59 to the 904L side of the fusion zone also, Mo has higher solubility in the Ni-based superalloy's liquid phase than the Fe-Ni based superalloy's liquid phase. Compare to other elements in the weld metal, Mo has a higher solidification temperature. Mo tends to segregate to the inter dendritic regions, which are the last to solidify, as the weld pool solidifies.

The Mo enrichment in the fusion zone is further enhanced by this segregation. The elemental concentrations in different zones of the dissimilar weld joint provided in TABLE 4. In order to ensure the accuracy, EDS analysis is conducted at various points within each zone, and the resulting averages, along with their standard deviations, are also presented in a TABLE 4. The fusion zone (FZ) (depicted in Fig. 5(a)) exhibits a finely structured equiaxed dendrite configuration. SEM analysis un-

TABLE 4

EDS Analysis of weld zone elemental composition (%)

| Type of Welding | Zone | Ni | Cr | Mo | Fe | Mn | Cu |
|---|---|---|---|---|---|---|---|
| HWTT with ERNiCrMo-13 | Weld center dendritic zone | 58.26 ± 0.8 | 23.53 ± 1.24 | 9.01 ± 1.26 | 7.92 ± 1.20 | 0.76 ± .08 | 0.61 ± 0.2 |
| | Weld center inter dendritic zone | 56.95 ± 1.2 | 24.14 ± 0.98 | 11.24 ± 0.88 | 7.07 ± 1.16 | 0.80 ± 0.06 | 0.72 ± 0.1 |
| | Weld center secondary phase | 37.02 | 23.64 | 32.06 | 05.02 | 0.78 | 0.48 |
| | Weld IF dendritic zone (Alloy 59 side) | 53.00 ± 1.12 | 23.46 ± 1.02 | 08.86 ± 0.9 | 12.18 ± 1.18 | 0.90 ± 0.06 | 0.81 ± 0.1 |
| | Weld IF inter dendritic zone (Alloy 59 side) | 48.89 ± 0.6 | 24.52 ± 1.28 | 12.47 ±1.08 | 11.34 ± 1.86 | 1.10 ± 0.04 | 0.74 ± 0.2 |
| | Weld IF dendritic zone (904L side) | 49.17 ± 1.68 | 22.84± 0.82 | 08.76 ± 0.28 | 17.26 ± 2.24 | 0.86 ± 0.08 | 0.68 ± 0.2 |
| | Weld IF inter dendritic zone (904L side) | 47.45 ± 2.12 | 23.65± 1.28 | 09.90 ±0.42 | 17.18 ±1.32 | 0.94 ±0.12 | 0.56 ±0.23 |

derlines the limited presence of secondary phases within the inter dendritic (ID) regions of the fusion zone. Furthermore, EDS examination (Fig. 5(i-ii)) validates the marginal elemental segregation stemming from minor deviations in elemental values, both within the inter dendritic and dendritic core regions. The SEM analysis reveals the presence of dendrites and arms within the weld zone, accompanied by thin Mo rich secondary phases. In the interface zone of 904L (Fig. 6a), secondary TCP phases are conspicuously absent. Similarly, secondary TCP phases are not observed on the alloy 59 side of the weld interface region (Fig. 6(b)). Fig. 6(i-ii) portrays the EDS point analysis of the WI of 904L, while Fig. 6(iii-iv) illustrates the EDS point analysis of alloy 59 WI. Fig. 6(i & ii) along with TABLE 4 collectively demonstrate minimal variation in alloying elements between the dendritic core and the inter dendritic region at the weld interface (WI) of the alloy 904L side. It is noteworthy that the 904L interface region is enriched with nickel content, a result of utilizing overmatching filler wire ERNiCrMo-13. Conversely, alloy 59 exhibits limited elemental variance on the weld interface side, signifying the absence of elemental segregation in line with the work done by Siva Kumar, N et al. [46].

The mechanisms of micro segregation in nickel alloy welding are closely related to the thermodynamics and kinetics of the solidification and diffusion processes. Factors such as the alloy composition, cooling rate, welding parameters, and post weld heat treatment can all influence the degree and extent of micro segregation. The heat input and cooling rate are key parameters in controlling the micro segregation in different alloy welds. Higher heat input in welding leads to a larger molten pool and longer solidification time. This extended solidification allows more time for diffusion and redistribution of alloying elements, reducing the extent of micro segregation. After solidification, diffusion processes can further affect the redistribution of alloying elements. Diffusion occurs at elevated temperatures, which are present during welding, and it can result in the migration of elements and the formation of concentration gradients within the

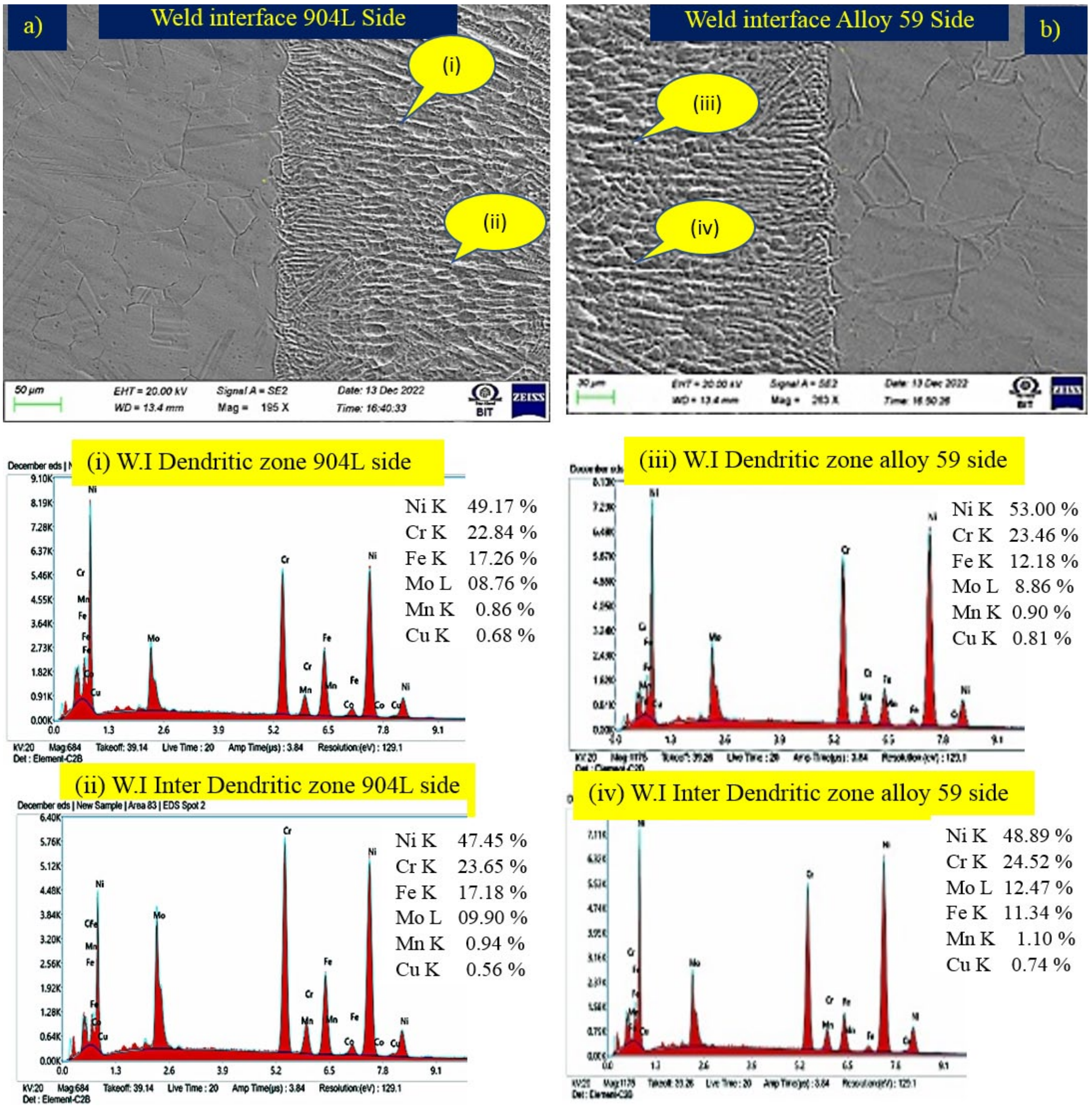

Fig. 6. SEM/EDS analysis of dissimilar weld made by HWTT- ERNiCrMo-13 Filler (a) SEM WI of 904L; (b) SEM WI of alloy 59; (i) EDS of WI- dendritic zone of 904L side (ii) EDS of WI inter-dendritic zone of 904L side; (iii) EDS of WI- dendritic core of alloy 59 side and (iv) EDS of WI inter-dendritic zone of alloy 59 side

microstructure. Faster cooling rates during welding, achieved through higher cooling rates or increased heat dissipation, can promote the formation of a finer microstructure with reduced segregation. Rapid cooling limits the diffusion of alloying elements and promotes a more homogeneous distribution within the solidified microstructure.

The HWTT is a unique technique that incorporates a filler wire, enhancing precision and accuracy. It is useful in welding at high temperatures, as the filler wire experiences a controlled draw-back mechanism, ensuring a steady and adequate wire feed. This dynamic modification enhances the weld quality resembling a responsive tap between heat and filler wire. This configuration effectively harnesses arc energy for swift localized melting, minimizing wasteful heat transfer into the surrounding base metal. The combination of reduced heat input and rapid cooling curtails the time available for alloying elements to segregate within the fusion region. Furthermore, the fine equiaxed grain microstructure leads to a significantly increased grain boundary area, which in turn curbs the segregation of deleterious low-melting-point constituents along these boundaries. Point analysis of the dissimilar weldment reveals minimal compositional disparities between the matrix and inter dendritic regions within the fusion zone (as depicted in Fig. 5(a)). The EDS analysis of Alloy 59, the 904L interface side, and the weld zone yielded significant findings. The concentration of Fe ranged from 11% to 13% at the Alloy 59 interface side, 7% at the weldment, and 18% at the 904L side, indicating substantial dilution of Fe in both the weldment and the Alloy 59 side interface. In contrast, the Cr content remained consistent, ranging from 23% to 25% on both the weldment and interface sides of the base metals. The Ni concentration varied from 48% to 58% on the weldment and Alloy 59 side, while it was 47% to 49% on the 904L side. These results suggest successful parameter selection and heat input, as Ni contributed to appropriate dilution, agreeing with a study by Banovic, S.W., DuPont, J.N. et al. [47]. The findings indicate significant Fe dilution, consistent Cr presence, and effective Ni dilution due to the chosen parameters and heat input. The presence of sparse, minute white phases observed within the inter dendritic regions is enriched with elements such as Mo, Cr, and Fe. This outcome likely stems from the slight segregation of Mo-rich phases, substantiated by the compositional differences in Mo content between the matrix and inter dendritic zones. This phenomenon can be attributed to the comparatively larger radii of Mo within the molten pool, leading to segregation during the concluding stages of solidification.

## 3.4. Mechanical properties

### 3.4.1. Micro hardness evaluation

The hardness measurements were conducted across the entire cross-sectional area of the coupons, which included the cap, middle, and root sections, for all weldments that utilized ERNiCrMo-13 filler. Assessments using Vickers micro hardness were performed, and the findings are summarized in TABLE 5.

TABLE 5

Hardness test results of Hot wire turbo TIG dissimilar weldments

| Weld zone | μVH (Avg) at Crest | μVH (Avg) at Centre | μVH (Avg) at Root |
|---|---|---|---|
| Base Metal 904L | 184 ± 6 | 182 ± 6 | 182 ± 6 |
| Weld Interface 904L | 204 ± 4 | 200± 4 | 200 ± 2 |
| Fusion Zone | 232 ± 5 | 228 ± 5 | 226 ± 5 |
| Weld Interface Alloy 59 | 212 ± 6 | 210 ± 6 | 208 ± 6 |
| Base Metal Alloy 59 | 200 ± 5 | 200 ± 5 | 200 ± 5 |

Upon examining the hardness plot in Fig. 7(a) it becomes evident that there is a gradual change in hardness values from the 904L side to the alloy 59 side. Upon careful examination of the hardness results, it is clear that the dissimilar fusion zone displays the highest average hardness (232 HV), surpassing that of the 904L base metal by 26% and exceeding that of the alloy 59 base metal by 16%. In Fig. 7(a), microstructure images are combined with graphs showing hardness values, giving a detailed view of how hardness changes in different parts. The

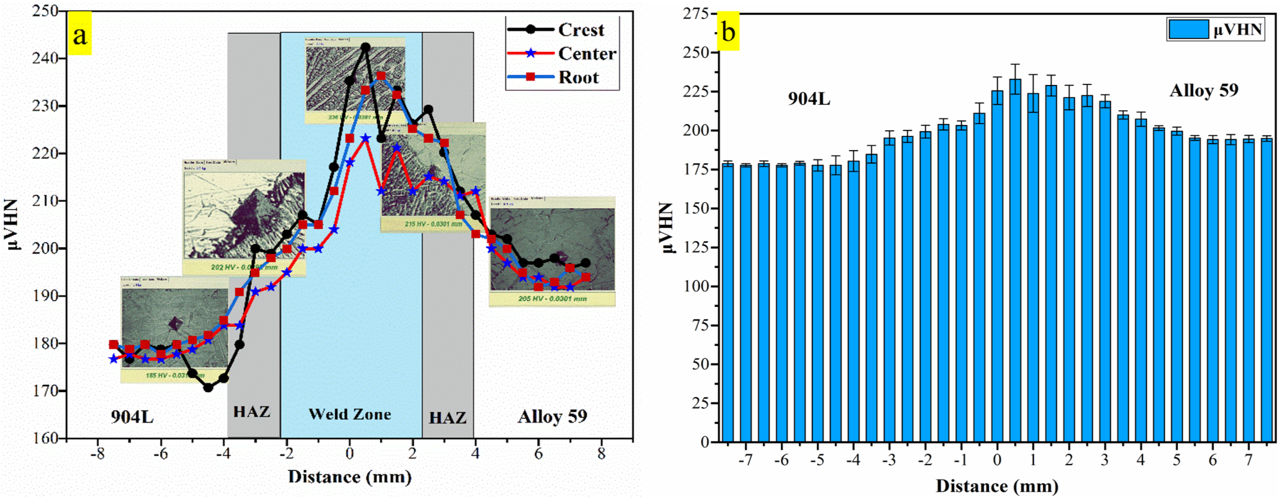

Fig. 7. a) Graphical representation of micro vickers hardness test of various regions of HWTT welded specimen, b) Column chart with error bar

microstructure includes the Interfaces of 904L and alloy 59 and base metals, as well as the welding zone. TABLE 5 depicts the mean hardness values of the sample at different positions: weld crest, center, and weld root. The values obtained at the 904L side align with the study by Ramkumar, K.D. et al. [48]. Fig. 7(b) presents a column chart accompanied by error bars, providing a visual representation of the data.

The hardness values of the Crest and center of the weldment were nearly identical, while the root slightly decreased. The gradual increase in micro hardness from the crest to the root in the fusion zone suggests a potential strengthening effect resulting from welding-induced grain refinement or altered microstructure However, the root area is typically cooled slower, resulting in lower hardness values. Overall the results show the feasibility of dissimilar welding between Alloy 59 and 904L, enabling consistent and reliable welds using HWTT.

### 3.4.2. Tensile strength

The tensile strength and ductility (expressed as the percentage of elongation) of the dissimilar weld joint using HWTT with ERNiCrMo-13 depicts in TABLE 6. The tensile failure of the dissimilar weld specimens illustrates in Fig. 8(a), 8(b), 8(c). The results of the tensile testing showed that the majority of the failures occurred on the side of the 904L base metal, away from the fusion zone (FZ). The data provided offer a comprehensive analysis of the mechanical characteristics of welded specimens under various conditions. Alloy 59 consistently demonstrates a yield strength of 380 MPa and an ultimate tensile strength (UTS) of 690 MPa. Additionally, it exhibits a significant elongation percentage of 40%. Similarly, 904L exhibits consistent yield strength and ultimate strength values of 280 MPa and 490 MPa, respectively, along with 36% elongation. When the welding process is completed, the mechanical properties of the welded material are slightly lower than those of the received material. The average yield strength is around 245 ± 10 MPa, the average ultimate tensile strength is around 610 ± 12 MPa, and the average elongation is around 38 ± 2%. The analysis of fracture indicates that failure primarily occurs on the Base Metal 904L side. The dissimilar weld fusion zone exhibited an average ultimate tensile strength of 610 MPa, surpassing that of the 904L base metal (490 MPa) but failing short of the alloy 59 base metal (690 MPa). The presence of a large number of well-formed equiaxed grains in the fusion zone greatly improves the tensile strength of the weld.

This is because these grains have consistent mechanical properties in all directions, unlike the unevenly spaced anisotropic columnar dendrites. As a result, the weld becomes even stronger [49]. The exceptional malleability of small equiaxed grains enables them to deform rapidly and endure contraction strains, thereby withstanding tensile loads and averting failure in the weld fusion zone.

Furthermore, the simultaneous reduction in heat input, elimination of micro segregation and increased cooling rates all contribute to the development of a more refined microstructure, which enhances the tensile properties in the fusion zone. In various studies, it has been observed that cryogenically treated tensile samples exhibited superior tensile performance compared to as welded tensile samples [50]. The shallow mode of cryogenic treatment induces stress relief by redistributing internal stresses through rapid cooling, improves dimensional stability by refining microstructures and reducing retained austenite, and enhances wear resistance by transforming retained austenite to martensite [51]. The use of deep cryogenic treatment (DCT) is notable as it offers a cost-effective and environmentally friendly approach to improve the overall mechanical properties. The shallow cryogenic treatment (SCT) in this work also yielded notable enhancements. The stress-strain curves for the as-welded, DCT, SCT samples are depicted in Fig. 8(d). The application of DCT results in an increased yield strength with an average value of 375 ± 5 MPa, ultimate tensile strength (UTS) of 680 ± 5 MPa, and elongation at 41 ± 1%). Fracture analysis consistently indicates failure occurring at the Base metal 904L side. The application of SCT leads to marginal decrease in the yield strength, with an average of 350 ± 6 MPa, an ultimate

TABLE 6

Tensile test results of dissimilar weldment

| Welding Specimen | Yield strength (MPa) | | Ultimate Tensile Strength (UTS) in MPa | | Percentage of Elongation | | Fractured Region |
|---|---|---|---|---|---|---|---|
| | Trial | Average | Trial | Average | Trial | Average | |
| Alloy 59 | 380 | 380 | 690 | 690 | 40 | 40 | — |
| 904L | 280 | 280 | 490 | 490 | 36 | 36 | — |
| As-Welded | 332 | 330 ± 6 | 624 | 625 ± 8 | 40 | 38 ± 2 | Fractured at Base Metal 904L side |
| | 336 | | 620 | | 36 | | |
| | 322 | | 630 | | 38 | | |
| Cryogenic Treated – Deep | 375 | 375± 5 | 684 | 680± 5 | 42 | 41 ± 1 | Fractured at Base Metal 904L side |
| | 380 | | 680 | | 40 | | |
| | 370 | | 676 | | 40 | | |
| Cryogenic Treated – Shallow | 356 | 350 ± 6 | 650 | 650 ± 6 | 39 | 40 ± 2 | Fractured at Base Metal 904L side |
| | 344 | | 656 | | 35 | | |
| | 350 | | 645 | | 40 | | |

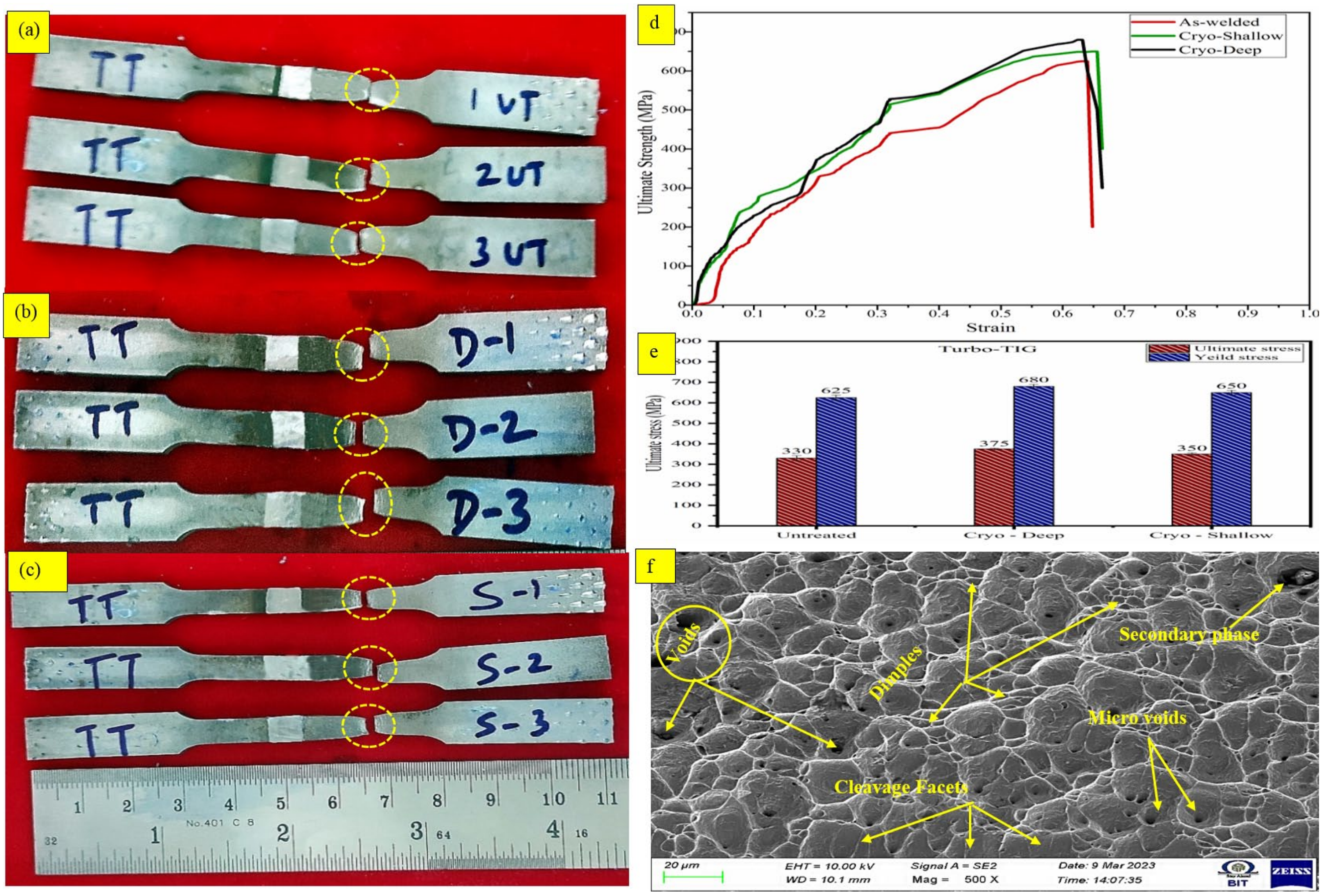

Fig. 8. Tensile tested specimen: (a) As-welded, (b) Cryogenic treated in deep mode, (c) Shallow mode, (d) Stress strain curve, (e) Error bar chart, (f) Fractography

tensile strength (UTS) of 650 ± 6 MPa, and an elongation of 40 ± 2. Upon further examination, the fracture analysis reveals that the failure occurred at the base metal 904L side. DCT yields superior tensile properties compared to SCT. According to the data presented in Fig8 (e) the ultimate strength of DCT is found to be 9.5% greater than that of the as-welded samples, and it exhibits a 4.5% increase compared to SCT samples, whereas the yield strength noticed 12% and 6.7% increased. The conditions of low thermal energy and restricted atomic movement at cryogenic temperature facilitate the formation of point defects and encourage the creation and buildup of dislocations in the crystal lattice, also, it promotes grain refinement in microstructure [52].

The refined microstructure can result in enhanced mechanical characteristic, including enhance resilience and malleability, as well as heightened resistance to fatigue. This phenomenon has significant implications for the mechanical characteristics of materials. To enhance the mechanical properties and elastic behavior of various materials cryogenic treatment techniques have become a highly effective method and are extensively employed by various industries. The DCT further enhances microstructure of the material, rendering it more imperious to corrosion and environmental deterioration. The DCT proved to be superior to the SCT in dissolving the brittle phases. In brief DCT improves the mechanical characteristics of welded specimens, resulting in enhanced yield strength, UTS, and ductility. Fractography images evaluating the failure mode through Fig. 8(f). The SEM Fractography clearly confirmed the ductile nature of the tensile fractures, as evidenced by the significant presence of micro voids and ductile ridges. These features indicate a failure mechanism involving the coalescence of micro voids. The prevalence of elongated dimples and the limited presence of cleavage facets provide additional evidence for the ductile failure mode [53]. The dimensions of the ductile dimples show heterogeneity in all Fractography samples.

### 3.4.3. Impact strength

The results of impact toughness for the dissimilar joint shown in TABLE 6. While Fig. 9(a) displays images of the specimens that fractured due to impact load. The recorded data of toughness (J) for the welded specimens provide information about the mechanical properties of various materials and welding conditions. The base metals, alloy 59 and 904L, consistently exhibit average toughness values of 90 J and 80 J, respectively. It is worth mentioning that the impact samples completely fractured during testing. Fig. 9(b) demonstrates that the toughness of the weld fusion zone (FZ) measured at 89 J is 2% lower than that of alloy 59 but 11.2% higher than that of 904L.

TABLE 6

Impact test results of dissimilar weldment

| Welding Specimen | Toughness (J) |
|---|---|
| Base Metal (Alloy 59) | 90 |
| Base Metal (AISI904L) | 80 |
| Hot wire-TIG ERNiCrMo-13 welding (As-Welded) | 81 |
| Hot wire-TIG ERNiCrMo-13 welding (Cryogenic Treated- Deep) | 89 |
| Hot wire-TIG ERNiCrMo-13 welding (Cryogenic Treated- Shallow) | 83 |

The difference is ascribed to the minimal micro segregation at both the fusion zone (FZ) and weld interfaces. Equiaxed grains with fine microstructures effectively resist abrupt loads. Equiaxed dendrites possess a structure that is more uniform in all directions compared to oriented dendrites. This leads to better mechanical properties, such as increased toughness and resistance to fatigue. There are significant differences observed when using HWTT with ERNiCrMo-13 filler both in its as-welded state and after cryogenic treatment. The as-welded specimen yields a toughness of 81 J, while 83 J is obtained after SCT. The toughness is shown to significantly improve 89 J after DCT illustrated in Fig. 9(b). Impact toughness of the weld joints treated with DCT significantly improves more than that of as-weld and SCT treated weldments. The DCT, which involves prolonged exposure to extremely low temperatures, can effectively refine the microstructure, reduce residual stresses, and enhance resistance to crack propagation [54,55]. These findings highlight the impact of cryogenic treatment on welding joint toughness, with more significant improvements resulting from deeper treatment. A ductile fracture mode characterized by micro voids, dimples, and numerous ductile tearing ridges is confirmed by SEM Fractography shown in Fig. 9(c) and 9(d). The ductile failure

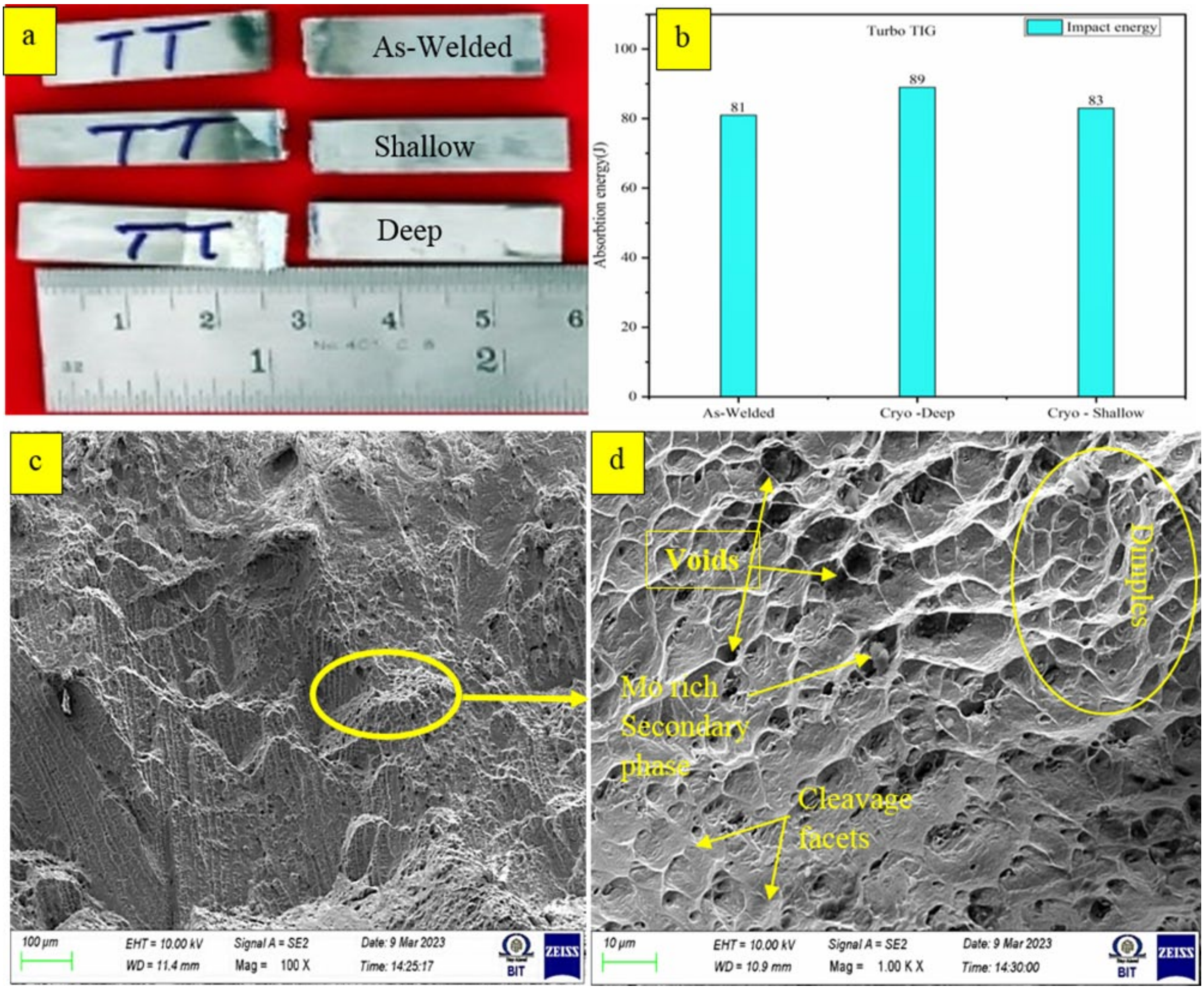

Fig. 9. (a) Impact tested specimen, (b) Graphical representation of absorbed energy, (c) Macro image of fractography, (d) SEM image fractography of impact specimen

mode is mostly supported by the presence of numerous ductile dimples, ductile tearing ridges, and fewer cleavage facets. These results also agree with the general increased impact toughness seen in the cryogenically treated specimens.

## 4. Conclusion

In this work the authors investigate the mechanical properties and microstructure characteristic of a dissimilar weld between alloy 59 and 904L. These welds are achieved through Hot Wire Turbo TIG (HWTT) welding using ERNiCrMo-13 filler wire. The key findings are as follows:

- The Hot Wire Turbo TIG process effectively joined superalloy 59 with 904L, producing defect-free welds and 0.6 mm depth of penetration using minimum heat input 0.61 KJ/mm and a higher speed of 130 mm/min observed by Macroscopic analysis.
- Microstructural analysis revealed a fine equiaxed columnar dendrites in the fusion zone, and columnar dendrites ensure clear interface between alloy 59 and 904L.The less heat input helps to faster cooling rate with separate Turbo power unit used to heat the wire half of its melting temperature in HWTT welding process.
- SEM/EDS analysis shows absence of secondary TCP phases in the inter dendritic region of the fusion zone, attributed to the effect of rapid cooling and reduced heat input. The findings of lower concentrations of Ni and Fe and higher concentrations of Mo content in the fusion zone are further supported by EDS line mapping.
- Tensile testing revealed alloy 59 produce superior tensile strength compared to 904L.Cryogenic treatment, especially in DCT demonstrated 9.5% greater than that of the as-welded samples and it exhibits 4.5% increase compared to SCT samples, whereas the yield strength noticed 12% to 6.7% increased. However cryogenic treatment showed limited impact on fracture locations maintaining fractures at the 904L side.
- Charpy impact toughness of the weld fusion zone (FZ) measured 89 J which is 2% lower than alloy 59 but 11.2% higher than 904L as DCT weldment.
- The hardness trend indicates that the fusion zone had the greater hardness values of 232 HV which was higher than the base metals. The range of hardness values at crest 232 ± 5 at root 226 ± 5. The observed increase in hardness in the fusion zone of ERNiCrMo-13 filler weldment attributed to the presence of the alloying element Mo.
- The presence of the crescent shaped phenomenon at 904L side of interface that extends into the fusion zone could lead to formation of intermetallic compounds, which could be reduce the ductility of the weldment and susceptible to cracking. Future research is recommended to optimize the hot wire temperature in HWTT to minimize the formation of these phases and enhance weld quality.

The HWTT welding process has shown potential in joining dissimilar materials, and the incorporation of Industry 4.0 concepts for process monitoring and optimization represents an exciting direction for future research. Its precise control, and high-quality weld outcomes make it suitable for integration with automated systems. Additionally, further investigation can be conducted to explore the optimization of cryogenic treatment parameters for dissimilar weldments of alloys 59 and 904L.

### Acknowledgement

The authors express their heartfelt thanks to the Center for Machining and Materials Testing (CMMT) for providing the testing facility and Prof M. Manikandan, Vellore Institute of Technology, Vellore, for his valuable inputs.

## REFERENCE

[1] https://www.vdmmetals.com/de/fileadmin/user_upload/Downloads/Data_Sheets/Data_Sheet

[2] P. Hübner, R. Behrens, H. Alves, D. Niespodziany, O. Sarrat, J. König, New Experiences with Explosion Clad Alloys UNS N06058 and UNS N06059. Ampp Corrosion, p. D031S034R005. AMPP, 2022.

[3] C. Agarwal Dinesh, W.R. Herda, J. Kloewer, Case histories on solving severe corrosion problems in the CPI by an advanced NiCrMo Alloy 59 UNS N06059. In Nace Corrosion, pp. NACE-00501. NACE, 2000.

[4] M. Chludzinski. R.E. Dos Santos C. Churiaque, M. Ortega-Iguña, J. M. Sánchez-Amaya, Pulsed laser welding applied to metallic materials – A material approach. Metals **11** (4), 640 (2021).

[5] W. Shi, J. Wang, R. Jiang, S. Xiang, Anticorrosion properties of the low-temperature glow plasma nitriding layer on aisi 904l austenitic stainless steel in hydrofluoric acid obtained at various nh3 pressures. Coatings **10** (12), 1156 (2020).

[6] D.D. Nage, V.S. Raja, Effect of nitrogen addition on the stress corrosion cracking behavior of 904 L stainless steel welds in 288 C deaerated water. Corros. Sci. **48** (8), 2317-2331 (2006).

[7] https://taiwan-plasma.com/product/Turbo-tig-welding-machin

[8] R. Sridhar, K.D. Ramkumar, N. Arivazhagan, Characterization of microstructure, strength, and toughness of dissimilar weldments of inconel 625 and duplex stainless steel SAF 2205. Acta Metall. Sin. (Engl. Lett.) **27**, 1018-1030 (2014).

[9] A.K. Maurya, C. Pandey, R. Chhibber, Dissimilar welding of duplex stainless steel with Ni alloys: a review. Int. J. Pres.Ves. Pip. **192**, 104439 (2021).

[10] G. Dak, C. Pandey, A critical review on dissimilar welds joint between martensitic and austenitic steel for power plant application. J. Manuf. Process. **58**, 377-406 (2020).

[11] L.D. Evjemo, T. Gjerstad, E.I. Grøtli, G. Sziebig, Trends in smart manufacturing: Role of humans and industrial robots in smart factories. Curr. Robot. Rep **1**, 35-41 (2020).

[12] Q. Wang, W. Jiao, P. Wang, Y. Zhang, A tutorial on deep learning-based data analytics in manufacturing through a welding case study. J. Manuf. Process. **63**, 2-13 (2021).

[13] A. Shaikh, S. Shinde, M. Rondhe, S. Chinchanikar, Machine learning techniques for smart manufacturing: a comprehensive review. Industry 4.0 and Advanced Manufacturing: Proceedings of I-4AM **2022**, 127-137 (2022).

[14] B. Wang, S.J. Hu, L. Sun, T. Freiheit, Intelligent welding system technologies: State-of-the-art review and perspectives. J. Manuf. Syst. **56**, 373-391 (2020).

[15] M. Arivarasu, D. Ramkumar Kasinath, A. Natarajan, Effect of continuous and pulsed current on the metallurgical and mechanical properties of gas tungsten arc welded AISI 4340 aeronautical and AISI 304 L austenitic stainless steel dissimilar joints. Mater. Res. **18** (1), 59-77 (2015).

[16] H. Naffakh, M. Shamanian, F. Ashrafizadeh, Dissimilar welding of AISI 310 austenitic stainless steel to nickel-based alloy Inconel 657. J. Mater. Process. Tech. **209** (7), 3628-3639 (2009).

[17] X. Gao, D. Ding, T. Bai, S. Katayama, Weld-pool image centroid algorithm for seam-tracking vision model in arc-welding process. IET Image Process. **5** (5), 410-419 (2011).

[18] M. Benakis, C. Du, A. Patran, R. French, Welding process monitoring applications and industry 4.0. IEEE 15th International Conference on Automation Science and Engineering (CASE), pp. 1755-1760, IEEE (2019).
DOI: https://doi.org/10.1109/COASE.2019.8843319

[19] S. Mahajan, R. Chhibber, Design and development of shielded metal arc welding (SMAW) electrode coatings using a CaO-CaF 2-SiO 2 and CaO-SiO 2-Al 2 O 3 flux system. J. Min. Met. Mat. S **71**, 2435-2444 (2019).

[20] G.K. Ahiale, Y.J. Oh, W.D. Choi, K.B. Lee, J.G. Jung, S.W. Nam, Microstructure and fatigue resistance of high strength dual phase steel welded with gas metal arc welding and plasma arc welding processes. Met. Mater. Int. **19,** 933-939 (2013).

[21] AkashHarendra Dagur, Ashwin Anil Kartha, MoharilAtharvaSubodh, C. Vishnu, D. Arun, M. Giridharan Vijay Kumar, Winston Sunny Abraham, Ankita Chatterjee, Jayanthi Abraham, J. Manuf. Process. **30**, 27-40 (2017).
DOI: https://doi.org/10.1016/j.jmapro.2017.09.001

[22] S. Varmaziar, H. Mostaan, M. Rafiei, M. Yeganeh, Welding and Corrosion Behavior of AISI H13 Welds: The Effect of Filler Metal on the Microstructural Evolutions. Arch. Metall. Mater. **66**, (2021).
DOI: https://doi.org /0.24425/amm.2021.136388

[23] K.A. Unocic, X. Chen, P.F. Tortorelli, Microstructural evaluation of welded nickel-based superalloy inconel 740H after creep testing. J. Min. Met. Mat. S **72** (5), 1811-1821 (2020).

[24] S.G.K. Manikandan, D. Sivakumar, K.P. Rao, M. Kamaraj, Effect of weld cooling rate on Laves phase formation in Inconel 718 fusion zone. J. Mater. Process. Tech. **214**,(2), 358-364 (2014).

[25] D.E. Villanueva, F.C.P. Junior, R.L. Plaut, A.F. Padilha, Comparative study on sigma phase precipitation of three types of stainless steels: austenitic, superferritic and duplex. Mater. Sci. Technol **22** (9), 1098-1104 (2006).

[26] W.A. Baeslack III, D.W. Becker, F.H. Froes, Advances in titanium alloy welding metallurgy. J. Min. Met. Mat. S **36** (5), 46-58 (1984).

[27] A. Evangeline, P. Sathiya, B. Arivazhagan, Laves phase formation and segregation of Nb in Ni–Cr–Mo superalloy over 316l by hot wire (HW) TIG cladding process. Arab. J. Sci. Eng **45**, 9685-9698 (2020).

[28] A.R. Farkoosh, M. Pekguleryuz, The effects of manganese on the T-phase and creep resistance in Al–Si–Cu–Mg–Ni alloys. Mater. Sci. Eng. A **582**, 248-256 (2013).

[29] J. Yan, M. Gao, X. Zeng, Study on microstructure and mechanical properties of 304 stainless steel joints by TIG, laser and laser-TIG hybrid welding. Opt. Laser. Eng. **48** (4), 512-517 (2010).

[30] K.D. Ramkumar, N. Arivazhagan, S. Narayanan, Effect of filler materials on the performance of gas tungsten arc welded AISI 304 and Monel 400. Mater. Design **40**, 70-79 (2012).

[31] S.E. Vahdat, S. Nategh, S. Mirdamadi, Microstructure and tensile properties of 45WCrV7 tool steel after deep cryogenic treatment. Mater. Sci. Eng. A **585**, 444-454 (2013).

[32] P. Baldissera, C. Delprete, Effects of deep cryogenic treatment on static mechanical properties of 18NiCrMo5 carburized steel. Mater. Design **30** (5), 1435-1440 (2009).

[33] H. Zhang, X. Yan, Z. Chen, M. Zhao, L. Tang, Y. Gao, J. Li, Effect of cryogenic treatment on wear resistance and microstructure of 42CrMo steel. Arch. Metall. Mater **67** (1), 127-135 (2022).
DOI: https://doi.org/10.24425/amm.2022.137481

[34] J. Li, J. Zhou, S. Xu, J. Sheng, S. Huang, Y. Sun, E.A. Boateng, Effects of cryogenic treatment on mechanical properties and micro-structures of IN718 super-alloy. Mater. Sci. Eng. A **707**, 612-619 (2017).

[35] M.J. Jang, H. Kwak, Y.W. Lee, Y. Jeong, J. Choi, Y.H. Jo, H.S. Kim, Plastic deformation behavior of 40Fe–25Ni–15Cr–10Co–10V high-entropy alloy for cryogenic applications. Met. Mater. Int. **25**, 277-284 (2019).

[36] P. Wach, A. Ciski, T. Babul, A. Kapuścińska, D. Oleszak, The application of deep cryogenic treatment to improve the properties of nitrided layers formed on X153CrMoV12 steel. Arch. Metall. Mater. **64** (1), (2019).

[37] https://www.sandmeyersteel.com/images/Alloy904L-SpecSheet.pdf

[38] M. Sathishkumar, M. Manikandan, Development of pulsed current arc welding to preclude carbide precipitates in hastelloy x weldment using ERNiCr-3. J. Mater. Eng. Perform. **29**, 5395-5408 (2020).

[39] C. Chen, C. Fan, X. Cai, Z. Liu, S. Lin, C. Yang, Arc characteristics and weld appearance in pulsed ultrasonic assisted GTAW process. Results. Phys. **15**, 102692 (2019).

[40] Q.J. Sun, S.B. Lin, C.L. Yang, G.Q. Zhao, Penetration increase of AISI 304 using ultrasonic assisted tungsten inert gas welding. Sci. Technol. Weld. Joi. **14** (8), 765-767 (2009).

[41] S. Lu, H. Fujii, K. Nogi, Marangoni convection and weld shape variations in Ar–O2 and Ar–CO2 shielded GTA welding. Mater. Sci. Eng. A **380** (1-2), 290-297 (2004).

[42] B.A. Kessal, C. Fares, M.H. Meliani, A. Alhussein, O. Bouledroua, M. François, Effect of gas tungsten arc welding parameters on the corrosion resistance and the residual stress of heat affected zone. Eng. Fail. Anal. **107**, 104200 (2020).

[43] A. Srikanth, M. Manikandan, Development of welding technique to avoid the sensitization in the alloy 600 by conventional Gas Tungsten Arc Welding method. J. Manuf. Process. **30**, 452-466 (2017).

[44] S. Kou, Y.K. Yang, Fusion-boundary macrosegregation in dissimilar-filler welds: Fundamental solidification and macrosegregation in welds made with filler metals different in composition from the workpiece are presented. Weld. J **86** (10) (2007).

[45] T. Soysal, S. Kou, D. Tat, T. Pasang, Macrosegregation in dissimilar-metal fusion welding. Acta Mater **110**, 149-160 (2016).

[46] N. Sivakumar, B.S. Gandhi, K.S. Kumar, B. Arulmurugan, Effect of constant current and pulsed current gas tungsten arc welding process on microstructure and mechanical properties of superalloy 59 joints. Mater. Res. Express **9** (4), 046525 (2022).

[47] S.W. Banovic, J.N. DuPont, A.R. Marder, Dilution and microsegregation in dissimilar metal welds between super austenitic stainless steel and nickel base alloys. Sci. Technol. Weld. Joi. **7** (6), 374-383 (2002).

[48] K.D. Ramkumar, J.L.N. Varma, G. Chaitanya, A. Choudhary, N. Arivazhagan, S. Narayanan, Effect of autogeneous GTA welding with and without flux addition on the microstructure and mechanical properties of AISI 904L joints. Mater. Sci. Eng. A **636**, 1-9 (2015). DOI: https://doi.org/10.1016/j.msea.2015.03.072

[49] B. Arulmurugan, M. Sathishkumar, D. Balaji, K. Muralikrishnan, S. Pranesh, V. Praveen, M. Manikandan, Development of arc welding technique to preclude microsegregation in the dissimilar joint of Alloy C-2000 and C-276. P. I. Mech. Eng. E. J. Pro **235** (5), 1408-1419 (2021).

[50] D.S. Kumar, S.S. Kumar, Influence of post weld cryogenic treatment on the ballistic penetration resistance of friction stir-welded AZ31B magnesium alloy. P. I. Mech. Eng. C. J. Pro **236**, (13), 7304-7318 (2022).

[51] H.T. Serindağ, G. Çam, Characterizations of microstructure and properties of dissimilar AISI 316L/9Ni low-alloy cryogenic steel joints fabricated by gas tungsten arc welding. J. Mater. Eng. Perform **32** (15), 7039-7049 (2023).

[52] P.J. Singh, S.L. Mannan, T. Jayakumar, D.R.G. Achar, Fatigue life extension of notches in AISI 304L weldments using deep cryogenic treatment. Eng. Fail. Anal. **12** (2), 263-271 (2005).

[53] B. Arulmurugan, D. Balaji, S. Rajkumar, M. Kamaraj, V. Mageshwaran, M. Sathishkumar, N. Arivazhagan, Influence of filler wire and welding process to mitigate the microsegregation of alloy C-2000 using continuous and pulsed current gas tungsten arc welding techniques. J. Mater. Eng. Perform. **30** (8), 6050-6067 (2021).

[54] P. Jovičević-Klug, B. Podgornik, Review on the effect of deep cryogenic treatment of metallic materials in automotive applications. Metals **10** (4), 434 (2020).

[55] M.I. Hussain, S. Khushnood, Studies on the effects of cryogenic cooling on microstructure and mechanical properties of plasma arc welded SS 316. Mater. Res. Express **10** (3), 036508 (2023).